Tunnelling and Underground Space Technology 142 (2023) 105420

Contents lists available at ScienceDirect

Tunnelling and Underground Space Technology incorporating Trenchless Technology Research

journal homepage: www.elsevier.com/locate/tust

Rock fracture mechanism of air-deck charge blasting considering the action effect of blasting gas

Chenxi Ding [a,c], Renshu Yang [a], Xinguang Zhu [b,*], Chun Feng [b], Jun Zhou [b]

[a] School of Civil and Resource Engineering, University of Science and Technology Beijing, Beijing 100083, China
[b] Key Laboratory for Mechanics in Fluid Solid Coupling Systems, Institute of Mechanics, Chinese Academy of Sciences, Beijing 100190, China
[c] Hubei Key Laboratory of Blasting Engineering of Jianghan University, Wuhan 430056, China

ARTICLE INFO

Keywords:
Blasting gas
Air-deck charge
Profile quality
Rock damage and fracture

ABSTRACT

This paper primarily focuses on examining the impact of blasting gas, studying the rock fracture mechanism of air-deck charge blasting, and analyzing the evolutionary characteristics of blasting stress, the law of damage distribution, and the fracture characteristics in rock specimens. Firstly, indoor blasting model experiments are conducted and analyzed by combining the computed tomography (CT) scanning method, three-dimensional (3D) reconstruction technology, and fractal damage theory. The experimental results indicate that the distribution characteristics of rock damage in air-deck charge blasting are mainly determined by factors such as charge segment position, air-deck length, and position. Next, a numerical simulation method based on the coupling analysis of Lagrangian finite element and Euler finite volume is proposed to enable the numerical simulation of rock blasting fracture while considering the action effect of blasting gas. The analysis of the numerical simulation results reveals that the rock failure near the blasthole, under the influence of blasting gas, is primarily due to tensile failure, whereas the rock failure in the distant area is predominantly caused by shear failure. Furthermore, during the process of rock fragmentation by blasting gas, the initial interaction between the blasting gas and rock is the main controlling factor for rock damage and failure, whereas the subsequent reflection and transmission of blasting gas have a relatively minor impact on rock damage and failure.

1. Introduction

Blasting stress wave and blasting gas serve as the primary driving forces for rock fragmentation during blasting (Yang et al., 2018). Over the course of several decades, the fundamental theory of rock blasting has reached a consensus regarding the comprehensive effect of blasting stress wave and blasting gas. According to this theory, the blasting stress wave triggers the initial crack formation around the blasthole (Zhu et al., 2008), while the blasting gas propels the expansion of certain initial cracks, leading to the formation of macroscopic crack zones (Li et al., 2006), ultimately resulting in rock fracture. In practical engineering, researchers and engineering technicians have introduced radial decoupling charge blasting technology (Ding et al., 2021; Yang et al., 2019) and axial decoupling charge blasting technology (Lou et al., 2020; Hayat et al., 2019), by leveraging the rock-breaking characteristics of blasting stress wave and blasting gas, as depicted in Fig. 1. Radial decoupling charge blasting technology is commonly employed for smooth blasting or pre-splitting of tunnels (Li et al., 2023; Han et al., 2020), while axial decoupling charge blasting technology, also known as air-deck charge blasting technology, finds widespread usage in open-pit bench blasting (Yin et al., 2021; Liu and Katsabanis, 2020). In such blasting engineering, it is hoped that the energy of explosives can be efficiently utilized, the blasting stemming size can be uniform, and the surrounding rock can be effectively protected, while avoiding situations such as excessive rock fragmentation, excess of vibration, and severe damage to the surrounding rock (Lin et al., 2021; Costamagna et al., 2018; Huo et al., 2023). Both blasting techniques primarily capitalize on the air's buffering effect within the blasthole, which mitigates the instantaneous expansion and impact of the blasting gas, thereby reducing the blasting impact, equalizing the pressure within the blasthole, and extending the duration of action. Currently, the mechanism and application research on radial decoupling charge blasting have attained a relatively advanced stage, whereas the mechanism research on air-deck charge blasting remains insufficient despite its extensive engineering application.

In the investigation of the air-deck charge blasting mechanism, Lou et al. (2018) derived a formula for calculating the initial impact pressure

* Corresponding author.
E-mail address: zhuxg@imech.ac.cn (X. Zhu).

https://doi.org/10.1016/j.tust.2023.105420
Received 23 July 2023; Received in revised form 31 August 2023; Accepted 18 September 2023
Available online 23 September 2023

on the blasthole wall in air-deck charge blasting based on the Starfield superposition principle. They also determined the distribution pattern of the initial impact pressure within the charge section. Yang et al. (2012) examined the distribution of blasthole pressure under various charge conditions and noted that the peak value of the initial impact pressure is situated at the center of the charge section, significantly higher than the peak value of pressure in the air-deck section. Lu and Hustrulid (2003), employing shock wave management theory and numerical simulation methods, investigated the propagation of sparse and reflected waves in the detonation products of air-deck charge blasting. They discovered that this wave propagation causes pressure unloading, resulting in high-strength tensile stress in the rock surrounding the blasthole and enhancing rock fragmentation. Wu et al. (2010) explored the mechanism of air-deck charge blasting in concrete materials using the HJC damage evolution model implemented within the LS-DYNA finite element program. They observed that as the length of the air-deck increased, the failure mode of concrete shifted from compressive shear failure to tensile failure. Gao et al. (2023) applied numerical simulation methods to examine the blasting performance when the air-deck is positioned at the bottom of the blasthole. The findings revealed that the air-deck at the bottom of the blasthole functions as a buffering medium, safeguarding the rock at the bottom of the blasthole. It redistributes the energy from the explosive blast, diminishes the peak pressure of the shock wave, and effectively mitigates excessive damage to the rock at the bottom of the blasthole. Through on-site blasting experiments, Gu et al. (2015) discovered that the air-deck charge structure prolongs the duration of the blasting gas action, achieves a more uniform distribution of blasting energy, reduces the instantaneous energy of blasting vibration, and contributes to better rock fragmentation outcomes. Yang et al. (2023) observed significant fractal characteristics in the blasting damage on both sides of the blasthole, with the degree of rock damage near the initiation point being the smallest and gradually increasing along the direction of detonation. Cheng et al. (2022) investigated the impact of the air-deck on the peak particle velocity (PPV) induced by blasting, utilizing on-site experiments and numerical simulations. They found that the air-deck charge plays a role in buffering the blasting effect on the blasthole wall, reducing the initial pressure and peak of the stress wave, thus achieving the objective of minimizing blasting vibrations.

In the aforementioned research on the mechanism of air-deck charge blasting, less attention has been given to the significant role of blasting gas in the fracture behavior of such blasting techniques. In this paper, a cavity charge structure was introduced based on a one-dimensional flow analysis of blasting gas. This structure regulates the spatial and temporal characteristics of blasting gas, leading to the observation of a “double peak” evolution pattern of blasting strain (Ding et al., 2022). The first peak is generated by the action of the blasting stress wave, while the second peak is a result of blasting gas effect. The engineering implementation of this cavity charge structure is the air-deck charge structure, which achieves the separation of the effects of the blasting stress wave and the blasting gas at the two-dimensional model experimental level. This offers a novel perspective for understanding the fracture mechanism of air-deck charge blasting. Building upon this foundation, this paper employs indoor three-dimensional model experiments to conduct air-deck charge blasting in sandstone specimens. It combines computed tomography (CT) scanning and three-dimensional reconstruction methods to quantitatively analyze the fracture and damage characteristics of air-deck charge blasting. Furthermore, utilizing the continuum-discontinuum element method (CDEM), the paper proposes a numerical simulation approach that couples the Lagrangian finite element and Euler finite volume methods. This simulation method enables the analysis of the evolution and rupture process of air-deck charge blasting, taking into account the influence of blasting gas.

2. Parameter design of the model experiment

To investigate the fracture mechanism of air-deck charge blasting, red sandstone is selected as the experimental material. The specimen, depicted in Fig. 2, is cylindrical with a diameter of 50 mm and a height of 100 mm. In the middle of the specimen, a prefabricated blasthole with a diameter of 3 mm and a depth of 60 mm is created. The basic mechanical parameters of the red sandstone specimen are presented in

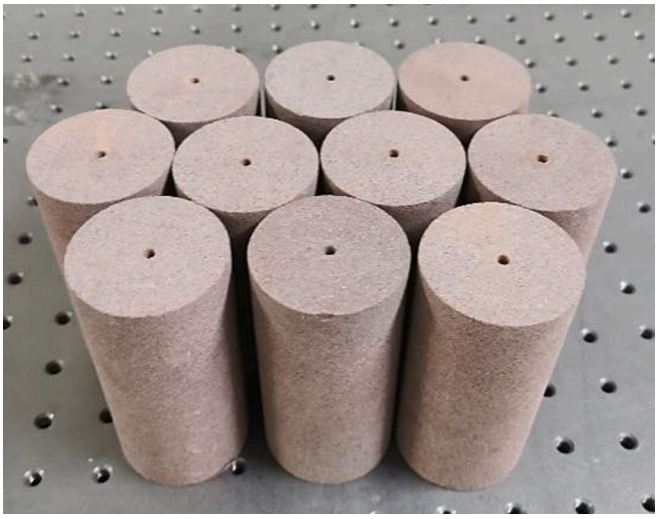

Fig. 2. Red sandstone specimens. (For interpretation of the references to colour in this figure legend, the reader is referred to the web version of this article.)

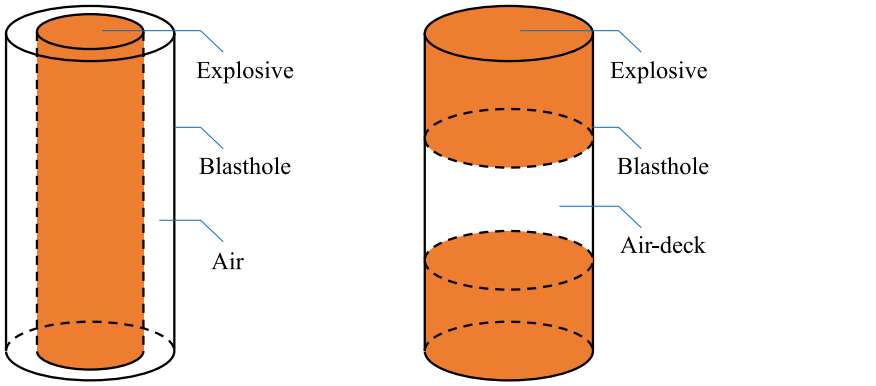

Fig. 1. Schematic diagram of the decoupling charge.

Table 1
Basic mechanical parameters of the red sandstone sample (Fang et al., 2023).

Density ($g \cdot cm^{-3}$)	Compressive strength (MPa)	Tensile strength (MPa)	P-wave velocity ($m \cdot s^{-1}$)
2.35	58.20	2.60	2432.00

Table 1. For the experiment, lead azide is utilized as the explosive, and the fundamental parameters of lead azide are outlined in Table 2. In order to ensure the same linear density of explosives in the charge segment, the explosives are loaded into a thin-walled plastic tube with an inner diameter of 1.8 mm, made into a strip shaped charge, and then placed in the corresponding position of the blasthole. A mixture of clay and glue is employed as the stemming medium for the blasthole. To secure and confine the specimen during the experiment, it is placed within the steel flange illustrated in Fig. 3, followed by tightening the bolt. The steel flange design can increase the transmission of blasting stress waves and reduce the interference of reflected stress waves on experimental results (Wang et al., 2020).

Fig. 4 illustrates the design of three experimental groups, namely A, B, and C, each with a stemming length charge length of 15 mm. The air-deck in each group has a total length of 30 mm. Among them, specimen A has its charge located in the upper part of the blasthole, specimen B in the middle part, and specimen C at the bottom part. To initiate the explosive, a high-voltage probe discharge method is employed during the experiment. Additionally, to visually depict the crack distribution post-blasting, CT scans are conducted on the red sandstone specimens. Utilizing a three-dimensional reconstruction method, a comprehensive three-dimensional fracture distribution map of the red sandstone is obtained.

3. Blasting fracture characteristics of the model experiment

3.1. Three-dimensional reconstruction of blast-induced cracks

To visually analyze the crack distribution post-blasting, CT scans are conducted on the red sandstone specimens. Each group of specimens yields 2000 CT scan slices along the blasthole axis, with a density of 20 slices per millimeter. For ease of experimental analysis, CT slice images are captured at 5 mm intervals from the upper surface to the lower surface of the specimen. Consequently, a total of 16 slice images are obtained for each group of specimens. By considering the distance s from the slice image to the upper surface of the specimen as a variable, the selected slice images for each group of specimens span from 0 mm to 75 mm from the upper surface. Partial slice images are presented in Fig. 5. From the figure, notable variations in crack distribution can be observed at different positions within the same specimen, and the fracture characteristics differ among specimens at the same position. The location of the air-deck significantly influences the fracture characteristics of the specimen.

The CT slice images are subjected to three-dimensional reconstruction (Ju et al., 2021)., resulting in the creation of a three-dimensional crack distribution map for the red sandstone specimen after blasting, depicted in Fig. 6. From the figure, notable disparities can be observed in the distribution of cracks following blasting, depending on the location of the explosives within the blasthole. Furthermore, to gain insights into the crack distribution along the blasthole axis, the specimen is segmented from top to bottom, with each segment measuring 15 mm in length. The analysis focuses on the first five segments from top to bottom. Among these segments, the stemming positions of the three specimen groups correspond to segment I, referred to as the "stemming segment". For Specimen A, the charge position aligns with segment II; for specimen B, it corresponds to segment III; and for specimen C, it corresponds to segment IV. To facilitate subsequent discussion, the segments associated with the charge positions of each specimen are collectively referred to as the "charge segment". Lastly, segment V of the three specimen groups is situated at the bottom of the blasthole and is referred to as the "bottom segment". Following the blasting process, cracks induced by the blasting primarily propagate along the diameter of the blasthole, with some extending through the specimen. Under the conditions of air-deck charge blasting, a set of divergent radial cracks emerges from the center of the blasthole, causing the fragmentation and separation of the rock mass.

Table 2
Basic parameters of lead azide (Ding et al., 2022).

Specific volume ($L \cdot kg^{-1}$)	Detonation temperature (℃)	Detonation velocity ($m \cdot s^{-1}$)
308	3050	4478

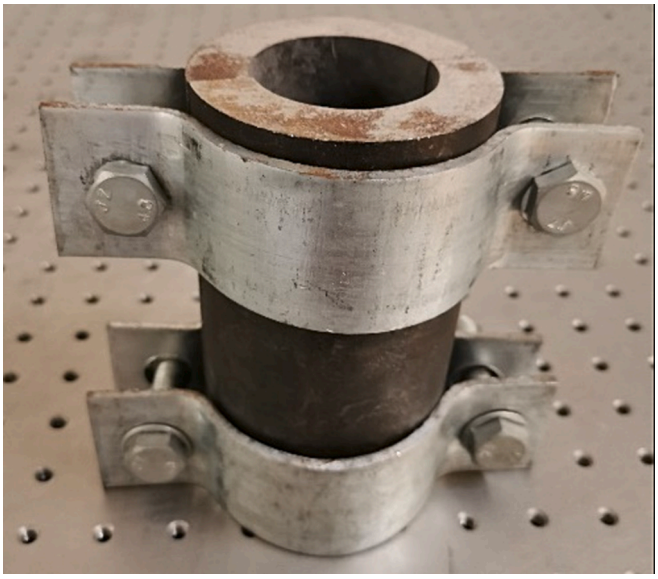

Fig. 3. The steel flange used during the experiment.

3.2. Damage characteristics of different segments

Previous research (Ding et al., 2021) has demonstrated that the crack distribution and the size of rock fragments resulting from blasting adhere to fractal characteristics. Fractal theory plays a crucial role in understanding the mechanism behind rock blasting. The fractal dimension reflects the effectiveness of complex shapes occupying space, and it is a measure of the irregularity of complex shapes. In the field of rock mechanics, the box counting dimension is a commonly employed method for calculating fractal dimensions. In three-dimensional space, the fractal dimension (D_b) of any non-empty bounded target set can be expressed as (Xie, 1997):

$$D_b = \lim_{k \to \infty} \frac{\lg N(\delta_k)}{-\lg \delta_k} \tag{1}$$

where D_b represents the fractal dimension; δ_k denotes the side length of the partitioned cube; $N(\delta_k)$ refers to the number of cubes required to cover the measured three-dimensional shape.

The three-dimensional reconstruction map of the cracks in the specimens after blasting, as shown in Fig. 6, is imported into the Matlab program. The number of cubes with different side lengths required to cover the blast-induced cracks is statistically analyzed, and the fractal dimension of the cracks in different specimens is calculated using Equation (1). The calculation of the overall fractal dimension of the three groups of specimens after blasting is presented in Fig. 7. The fractal dimension of the three-dimensional cracks in specimen A, specimen B and specimen C are 2.134, 2.286 and 2.297, respectively. It is observed

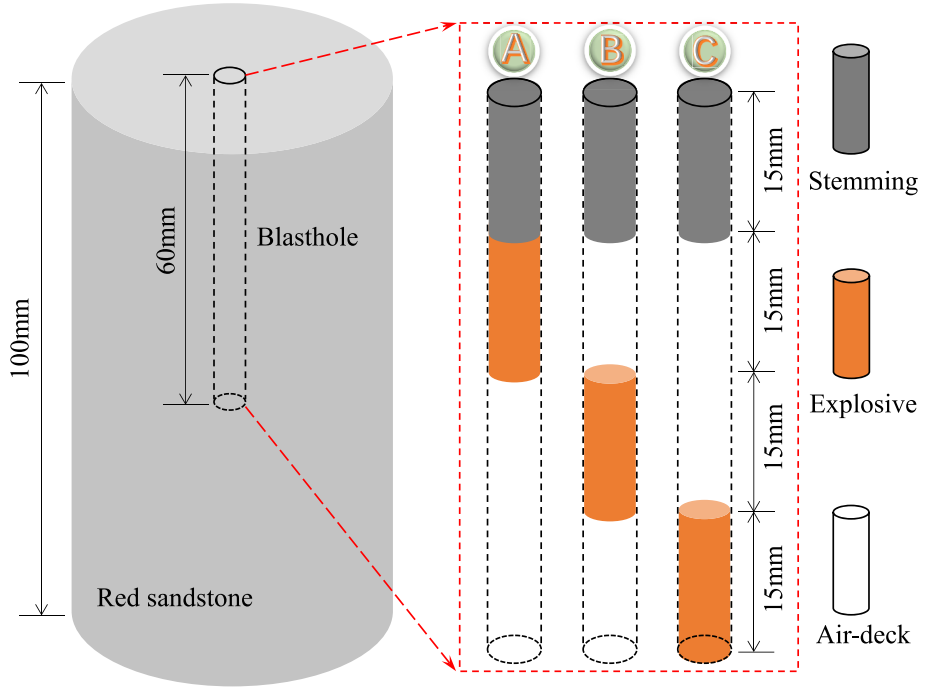

Fig. 4. Schematic diagram of the charge structure in the red sandstone specimen. (For interpretation of the references to colour in this figure legend, the reader is referred to the web version of this article.)

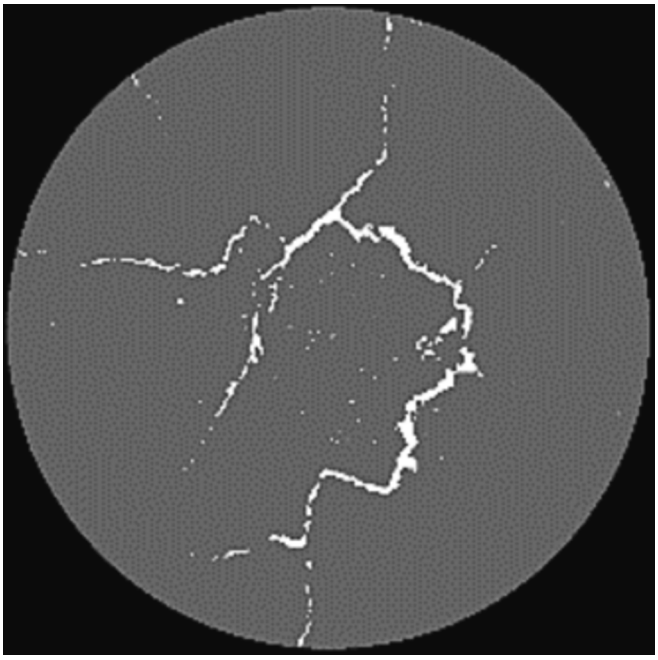

Fig. 5. CT slice images at different positions along the blasthole axis post-blasting.

that the overall fractal dimension of the three-dimensional cracks after blasting gradually increases as the charge segment moves downward from specimen A to specimen C. Furthermore, the fractal dimension of the cracks in different segments of the three groups of specimens is also calculated, and the corresponding fractal dimension values are listed in Table 3.

The relationship between the internal damage degree and the fractal dimension of cracks in rock can be described by the following equation:

$$\omega = \frac{D_b - D_0}{D_b^{max} - D_0} \tag{2}$$

where ω represents the damage degree of rock under the blasting load; D_b is the fractal dimension of three-dimensional cracks in rock after blasting; D_0 denotes the fractal dimension of three-dimensional (3D) cracks in rock before blasting. In this experiment, the red sandstone specimen is intact and dense prior to blasting, thus $D_0 = 0$; D_t^{max} is the fractal dimension under the condition of complete damage and failure; for three-dimensional problems, D_t^{max} is equal to 3.

According to Equation (2), the fractal dimension shows a linear relationship with the internal damage degree of rock. Based on the overall fractal dimension of the three-dimensional cracks after blasting and Equation (2), the overall damage degrees of specimen A, specimen B and specimen C are determined to be 0.711, 0.762, and 0.766, respectively. Specimen A exhibits the lowest overall damage degree, while specimen C shows the highest overall damage degree. This indicates that as the charge segment moves down the blasthole, the fragmentation and damage of the specimen become more severe. Furthermore, by combining the data from Table 3 with Equation (2), the damage degrees of different segments in the three groups of specimens can be determined, as depicted in Fig. 8. There are notable disparities in the damage degree among the different segments. Specifically, the charge segment (segment IV) of specimen C exhibits the highest damage degree at 0.815, whereas the stemming segment (segment I) of specimen C shows the lowest damage degree at only 0.672. These findings highlight the significant influence of the position of the charge and air-deck on the blasting damage. The subsequent analysis focuses on comparing and examining the distinct damage characteristics of the stemming segment, charge segment, and bottom segment in the three groups of specimens.

(1) Charge segment.

The charge segments in specimens A, B, and C correspond to segment II, III and IV, respectively. Although they are all charge segments, the damage degree of the charge segment in specimen A is the smallest, measuring 0.685. In contrast, the damage degree of the charge segment in specimen C is the highest, measuring 0.815. The damage degree of the charge segment in specimen B falls in between, measuring 0.769. The

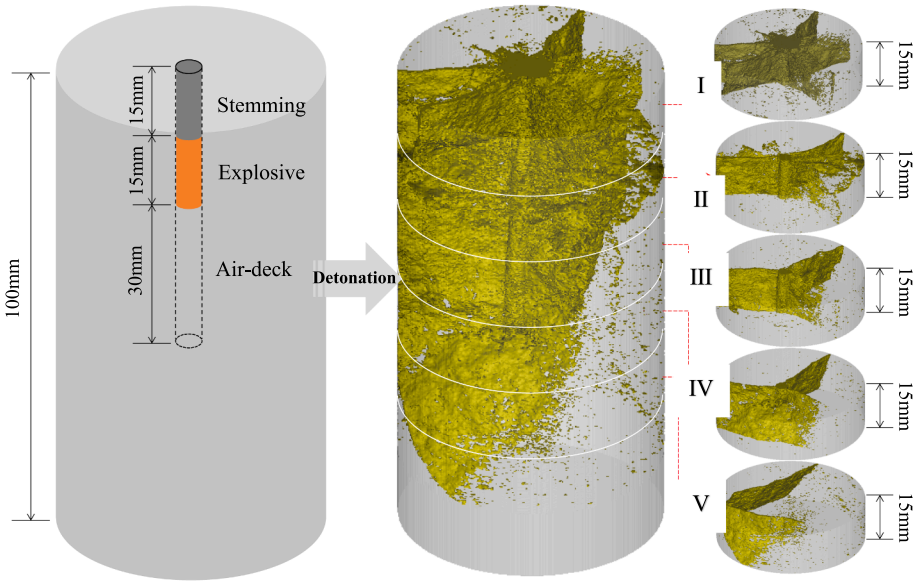

(a) Specimen A

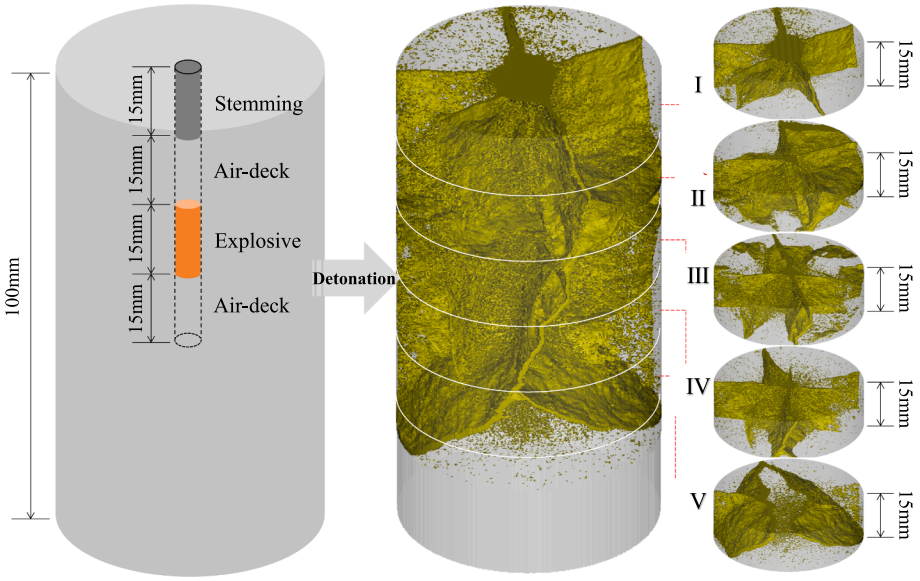

(b) Specimen B

Fig. 6. Three-dimensional reconstruction of blast-induced cracks in specimens post-blasting.

distribution characteristics of this type of damage primarily depend on factors such as the contribution of blasting stress waves, the stemming adjacent to the explosive, and the differences in the position and length of the air-deck.

Blasting stress wave and blasting gas serve as the primary driving forces for rock fragmentation during blasting. In Fig. 9, it can be observed that the explosives in the three groups of specimens make direct contact with the rock on the blasthole wall. The blasting stress wave, generated upon detonation of the explosives, directly impacts the blasthole wall, resulting in the formation of cracks. In the case of specimens A and B, the circumferential direction of the explosive directly interacts with the rock, while the upper and lower sides of the explosive do not make contact. Consequently, the contribution of blasting stress waves to rock fragmentation can be considered similar for specimens A and B. Therefore, the variations in the final fragmentation and damage characteristics are primarily attributed to the different effects of the blasting gas. In the case of specimen A, there is a 15 mm-long stemming positioned above the explosive and a 30 mm-long air-deck below it. After the detonation of explosives, two main factors come into play. Firstly, the blasting gas rapidly dissipates and compresses the air in the air-deck segment below. Secondly, the upper part of the explosive makes contact with the stemming material, a mixture of clay and glue, which exhibits some degree of compressibility. As a result of the impact and compression caused by the blasting gas, the stemming experiences significant compression, thereby absorbing a greater amount of energy from the blasting gas. It is the combined influence of these two factors that weakens the effect of the blasting gas on the charge segment of specimen A, leading to a lower damage degree. In the case of specimen

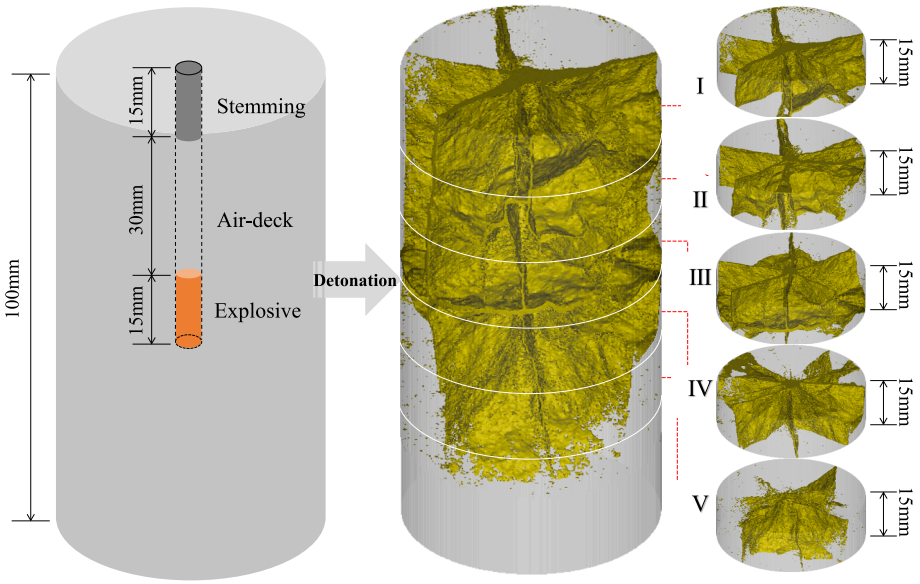

(c) Specimen C

Fig. 6. (*continued*).

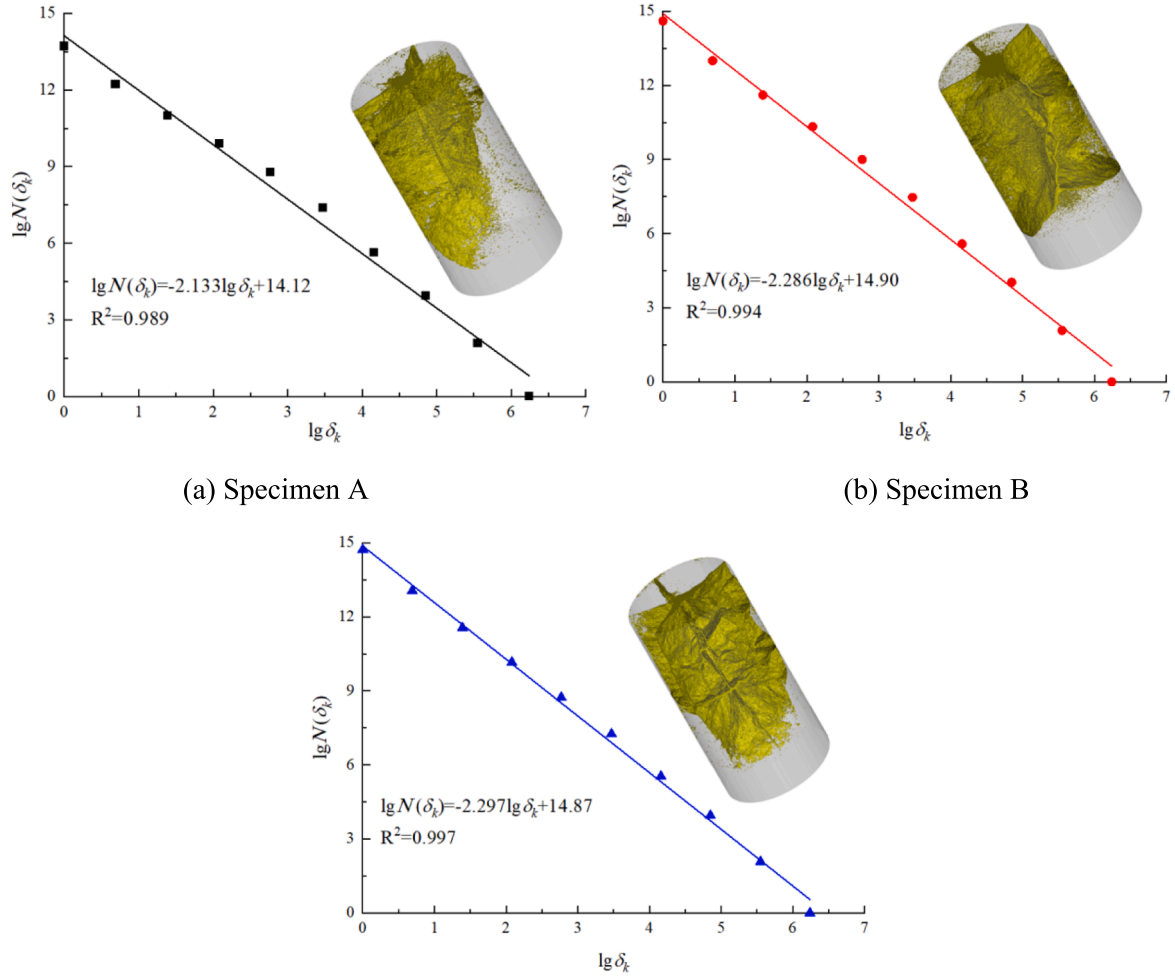

(a) Specimen A

(b) Specimen B

(c) Specimen C

Fig. 7. Calculation of the overall fractal dimension of three-dimensional cracks after blasting.

Table 3
Fractal dimension of the cracks in different segments of the three groups of specimens.

Segement	Specimen A	Specimen B	Specimen C
I	2.096	2.090	2.017
II	2.056	2.142	2.072
III	2.084	2.307	2.205
IV	2.152	2.264	2.446
V	2.133	2.341	2.319

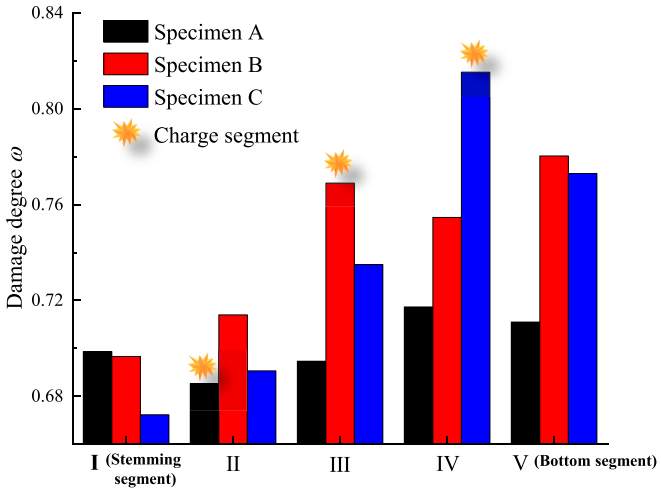

Fig. 8. Damage degrees of different segments in the three groups of specimens.

B, there is a 15 mm-long air-deck on both sides of the explosive. After the detonation of the explosive, the blasting gas escapes from both sides. In comparison to specimen A, the air-deck on the upper side of the charge segment in specimen B provides a certain buffering effect on the energy release of the blasting gas. However, the energy absorption effect of the blasting gas in specimen B is lower than that of the stemming on the upper side of specimen A. Consequently, a relatively higher amount of energy is utilized for the fragmentation of the charge segment in segment B, leading to greater damage compared to specimen A. In the case of specimen C, both the circumferential and lower sides of the explosive come into direct contact with the rock. This makes the charge segment of specimen C more significantly influenced by the blasting stress wave compared to specimen A and specimen B. Additionally, after the detonation of explosives in specimen C, the blasting gas can only freely escape towards the upper part of the charge segment, while other directions experience direct impact from the blasting gas. As a result, the charge segment of specimen C is subjected to more severe effects from the blasting stress waves and blasting gas compared to the charge segments of specimen A and specimen B, resulting in the highest level of damage observed in the charge segment of specimen C.

(2) Stemming segment.

The damage degrees of the stemming segment in specimen A, specimen B, and specimen C are 0.699, 0.697, and 0.672, respectively. Specimen A exhibits the highest damage degree in its stemming segment, while specimen C has the lowest. In the case of specimen A, the stemming is in direct contact with the explosive, subjecting the surrounding rock and stemming segment to the direct impact of both the blasting stress wave and blasting gas without any buffering. Consequently, the stemming segment in specimen A sustains greater damage compared to that of specimen B and specimen C. Conversely, specimen B and specimen C feature an air-deck between the explosive and the stemming, which mitigates the impact of the blasting stress wave and blasting gas on the stemming segment, resulting in a lower damage degree. Furthermore, specimen C possesses a longer air-deck above the explosives, leading to the least damage in the stemming segment among the three specimens.

(3) Bottom segment.

The damage degrees of the bottom segment in specimen A, specimen B, and specimen C are 0.711, 0.780, and 0.773, respectively. Specimen A exhibits the smallest damage degree in its bottom segment, while specimen B has the largest, and specimen C falls in between. In specimen A, the length of the air-deck below the explosive is twice that of specimen B, resulting in a more significant buffering effect on the escape and impact of the blasting gas. Consequently, the damage degree of the bottom segment in specimen A is significantly lower than that in specimen B. The analysis also reveals that the bottom segment of specimen C experiences both the effects of blasting stress waves and direct impact of blasting gas, with the intensity of the impact expected to be considerably greater than that in specimen B. However, the damage degree of the bottom segment in specimen C is smaller than that in specimen B. This is because rock fragmentation under blast loading depends not only on the intensity of the blasting stress wave and blasting gas but also on the duration of their action. The generation and action process of the blasting stress wave are transient, while the intensity and duration of the blasting gas can be controlled through the air-deck. In specimen C, the impact of the blasting gas on the bottom of the blasthole is transient, characterized by high intensity but short duration. It lacks sustained power for initiating damage and propagating cracks. On the other hand, in specimen B, the blasting gas acts on the bottom segment after being buffered by the air-deck, which reduces the impact strength but prolongs the duration of action. This extended action time is beneficial for initiating damage and facilitating continuous crack propagation. As a result, the damage degree in the bottom segment of specimen C is lower compared to specimen B. It is worth noting that the comparison between specimen A and specimen B also suggests the presence of an optimal range for the length of the air-deck, which should be determined based on engineering requirements.

Further comparison is made regarding the damage degrees of the two air-deck segments (segment II and segment IV) in specimen B. In specimen B, segment II and segment IV are positioned symmetrically around the explosive, but their damage degrees exhibit significant differences. The damage degrees of segment II and segment IV are 0.714 and 0.755, respectively. This disparity can be primarily attributed to the contrasting material properties present in the stemming segment (segment I) and the bottom segment (segment V) of the blasthole. The stemming segment is filled with a compressive stemming medium, which effectively absorbs and compresses the blasting energy, thereby reducing the energy available for crushing the rock in segment II. On the other hand, the bottom segment, being composed of hard and relatively non-deformable rock material, possesses limited capacity for absorbing blasting gas energy. Consequently, a greater proportion of the blasting gas energy is utilized for rock fragmentation in segment IV.

4. Proposal of the numerical simulation method

Based on the aforementioned experimental analysis, it is evident that the blasting gas assumes a predominant role in determining the ultimate failure pattern of the specimen during air-deck charge blasting. To delve deeper into the dynamic evolution process of blasting gas in air-deck charge blasting, this study introduces a numerical calculation approach that combines the Lagrangian finite element method with the Eulerian finite volume method within the computational framework of the continuum-discontinuum element method (CDEM) (Zhu et al., 2021; Li et al., 2004). This computational method enables the numerical simulation of the progressive damage evolution of rock subjected to the influence of blasting gas.

4.1. Characterization of solid deformation

The computation of element stress and node deformation force in the

Lagrangian finite element method is performed incrementally, as shown in Equation (3).

$$\begin{cases} \Delta\boldsymbol{\varepsilon}_i = \boldsymbol{B}_i \Delta\boldsymbol{u}_e \\ \Delta\boldsymbol{\sigma}_i = \boldsymbol{D}\Delta\boldsymbol{\varepsilon}_i \\ \boldsymbol{\sigma}_i^{\mathrm{t}} = \boldsymbol{\sigma}_i^{o} + \Delta\boldsymbol{\sigma}_i \\ \boldsymbol{\sigma}_i^{\mathrm{n}} = f(c_1, c_2, \ldots) \\ \boldsymbol{F}_e = \sum_{i=1}^{N} \boldsymbol{B}_i^T \boldsymbol{\sigma}_i^n w_i J_i \end{cases} \tag{3}$$

where $\boldsymbol{B}_i$, $\Delta\boldsymbol{\varepsilon}_i$, $\Delta\boldsymbol{\sigma}_i$, w_i and J_i correspond to the strain matrix, incremental strain tensor, incremental stress tensor (Pa), integral coefficient and Jacobi determinant of Gauss point i, respectively; $\boldsymbol{\sigma}_i^n$ and $\boldsymbol{\sigma}_i^o$ represent the stress tensors at the current and previous time steps of Gaussian point i (Pa), $\boldsymbol{\sigma}_i^t$ denotes the tentative stress tensor at Gaussian point i (Pa); $\boldsymbol{D}$, $\Delta\boldsymbol{u}_e$ and $\boldsymbol{F}_e$ represent the elastic matrix of the element (Pa), the incremental displacement vector of the node (m), and the deformation force tensor of the node (N), respectively; N indicates the number of Gaussian points.

After computing the node deformation force, it is also necessary to calculate the resultant force acting on the node, which can be expressed as:

$$\boldsymbol{F} = \boldsymbol{F}^E + \boldsymbol{F}^e + \boldsymbol{F}^d \tag{4}$$

where F represents the resultant force of the node (N); $\boldsymbol{F}^E$ denotes the external force of the node (N); $\boldsymbol{F}^e$ is the deformation force of the node; and $\boldsymbol{F}^d$ represents the damping force of the node (N).

The node motion is calculated using the Euler interpolation method, which can be expressed as:

$$\begin{cases} \boldsymbol{a} = \boldsymbol{F}/m \quad \boldsymbol{v} = \sum_{t=0}^{T_{now}} \boldsymbol{a}\Delta t \\ \Delta\boldsymbol{u} = \boldsymbol{v}\Delta t \quad \boldsymbol{u} = \sum_{t=0}^{T_{now}} \Delta\boldsymbol{u} \end{cases} \tag{5}$$

where $\boldsymbol{a}$ represents the node acceleration (m/s^2); $\boldsymbol{v}$ denotes the node velocity; $\Delta\boldsymbol{u}$ is the node displacement increment (m); $\boldsymbol{u}$ represents the total node displacement (m); m denotes the node mass (kg), and Δt is the calculation time step (s). By iteratively solving equations (3), (4), and (5), an explicit solution for the rock specimens can be obtained.

4.2. Description of blasting gas

The Euler finite volume method utilizes the compressible two-medium hydrodynamic model as the fundamental dynamic equation, which can be represented by Equation (6) and Equation (7).

$$\frac{\partial U}{\partial t} + \frac{\partial F}{\partial x} + \frac{\partial G}{\partial y} + \frac{\partial H}{\partial z} = S(U) \tag{6}$$

$$\frac{\partial}{\partial t}\begin{pmatrix} \rho \\ \rho u \\ \rho v \\ \rho w \\ E \\ \alpha_1\rho_1 \\ \alpha_1 \end{pmatrix} + \frac{\partial}{\partial x}\begin{pmatrix} \rho u \\ \rho u^2 + p \\ \rho uv \\ \rho uw \\ u(E+p) \\ \alpha_1\rho_1 u \\ \alpha_1 u \end{pmatrix} + \frac{\partial}{\partial y}\begin{pmatrix} \rho v \\ \rho uv \\ \rho v^2 + p \\ \rho vw \\ v(E+p) \\ \alpha_1\rho_1 v \\ \alpha_1 v \end{pmatrix} + \frac{\partial}{\partial z}\begin{pmatrix} \rho w \\ \rho uw \\ \rho vw \\ \rho w^2 + p \\ w(E+p) \\ \alpha_1\rho_1 w \\ \alpha_1 w \end{pmatrix} = \begin{pmatrix} 0 \\ 0 \\ 0 \\ 0 \\ 0 \\ 0 \\ \alpha_1 \nabla\cdot V \end{pmatrix} \tag{7}$$

where:

$$\boldsymbol{U} = (\rho, \rho u, \rho v, \rho w, E, \alpha_1\rho_1, \alpha_1)^T$$

$$\boldsymbol{F} = (\rho u, \rho u^2 + p, \rho uv, \rho uw, u(E+p), \alpha_1\rho_1 u, \alpha_1 u)^T$$

$$\boldsymbol{G} = (\rho v, \rho uv, \rho v^2 + p, \rho vw, v(E+p), \alpha_1\rho_1 v, \alpha_1 v)^T$$

$\boldsymbol{H} = (\rho w, \rho uw, \rho vw, \rho w^2 + p, w(E+p), \alpha_1\rho_1 w, \alpha_1 w)^T$, which represent the conserved variables and fluxes in three directions; $S = (0, 0, 0, 0, 0, 0, \alpha_1 \nabla\cdot V)^T$ denotes the source phase; E is the total energy (J), including kinetic energy and internal energy, $E = \rho(e + \frac{1}{2}(u^2 + v^2 + w^2))$.

It should be noted that the medium consists of two fluid substances, where α_1 and α_2 represent the volume fractions of the two media, with the condition $\alpha_1 + \alpha_2 = 1$. Additionally, ρ_1 and ρ_2 denote the densities of the two media. The average parameters of the mixed medium satisfy the following conditions:$\rho = \sum_{j=1}^{2}\alpha_j\rho_j$, $\rho u = \sum_{j=1}^{2}\alpha_j\rho_j u_j$, $\rho e = \sum_{j=1}^{2}\alpha_j\rho_j e_j$.

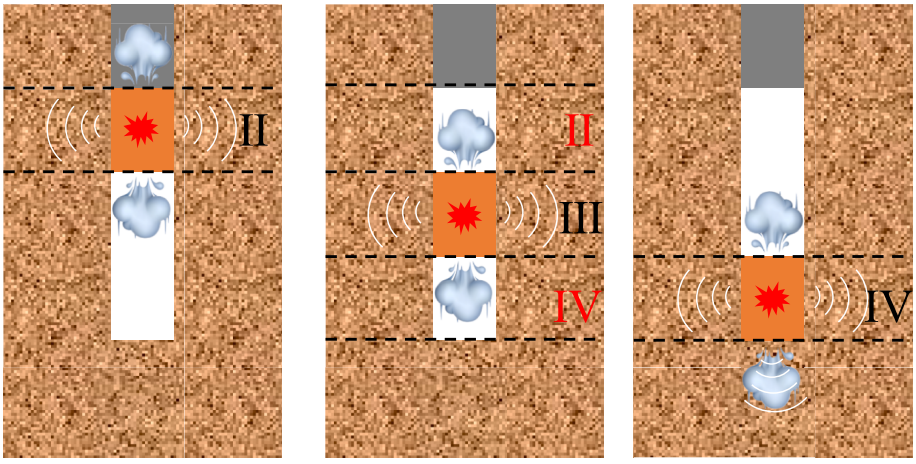

(a) Specimen A (b) Specimen B (c) Specimen C

Fig. 9. Schematic diagram illustrating the interaction between blasting stress wave and blasting gas in rock fragmentation.

The models described above need to be complemented by appropriate equations of state to form a closed mathematical system. For explosives, the JWL equation of state or Landau equation of state is utilized, while the adiabatic expansion equation is employed for air.

The software applies the finite volume method to solve the dynamic equation, uses the projection algorithm to handle the time step stiffness problem, utilizes the approximate Riemann solver Kurganov algorithm to calculate the numerical flux, and ensures second-order space–time accuracy through the use of the MUSCL method and the second-order Runge Kutta method.

4.3. Solution of gas–solid coupling

The Lagrange mesh-based finite element method is suitable for characterizing the dynamic behavior of solid materials, while the Euler mesh-based finite volume method is suitable for characterizing the dynamic behavior of fluids. By coupling these two methods, it becomes possible to simulate the deformation and damage of rocks under the influence of blasting gas. In this coupling, the Euler finite volume method primarily handles the calculation of flow field energy, pressure, velocity, composition and other physical quantities. On the other hand, the Lagrange finite element method is responsible for calculating displacement, velocity, stress, strain, damage, and other physical quantities. Pressure and velocity are variables that exist in both the Euler and Lagrange solutions. The coupling of the Euler and Lagrange algorithms aims to facilitate the transfer of pressure and velocity between the two algorithms.

Assuming that the inner wall of the blasthole undergoes small deformation due to the blasting gas, it can be considered as a solid wall boundary for the Lagrangian material in the Euler region calculation. Similarly, the Euler flow field serves as a pressure boundary for the Lagrangian region calculation. In this study, the pressure exerted by the blasting gas on the inner wall of the blasthole is calculated using an interpolation method.

Fig. 10 illustrates the pressure interpolation calculation diagram at the fluid–structure interaction boundary. The Euler mesh covers the inner space of the blasthole, while the Lagrangian mesh divides the surrounding rock. At time step t^n, the blasting gas pressure at Euler node i and its position in the Lagrangian element are known. The first step is to vertically project the Euler node i onto the free surface of the Lagrange element where it is located. This free surface refers to the empty plane of the Lagrange element at the boundary, which is an edge in the two-dimensional case and a face in the three-dimensional case. The projection point, denoted as i', is obtained. Subsequently, the blasting gas pressure at point i' is interpolated and applied to each node on the free surface using the following equation.

$$p_j = N_j p_i \tag{8}$$

where p_j represents the pressure of the jth node on the free surface of the Lagrange element (Pa); N_j denotes the shape function on a free surface; and p_i is the blasting gas pressure on the vertical projection point (Pa), which is directly inherited from the blasting gas pressure at Euler node i.

By multiplying the blasting gas pressure on the free surface by the corresponding node area and incorporating it into the variable $\boldsymbol{F}^E$ in Equation (4), the gas pressure in the Euler flow field can be applied to the Lagrangian solid as a surface force. This enables the coupling calculation between the two methods. The flowchart of the coupling algorithm of Lagrangian finite element and Euler finite volume under CDEM framework is shown in Fig. 11.

4.4. Validation of the numerical method

In order to verify the effectiveness of the gas–solid coupling

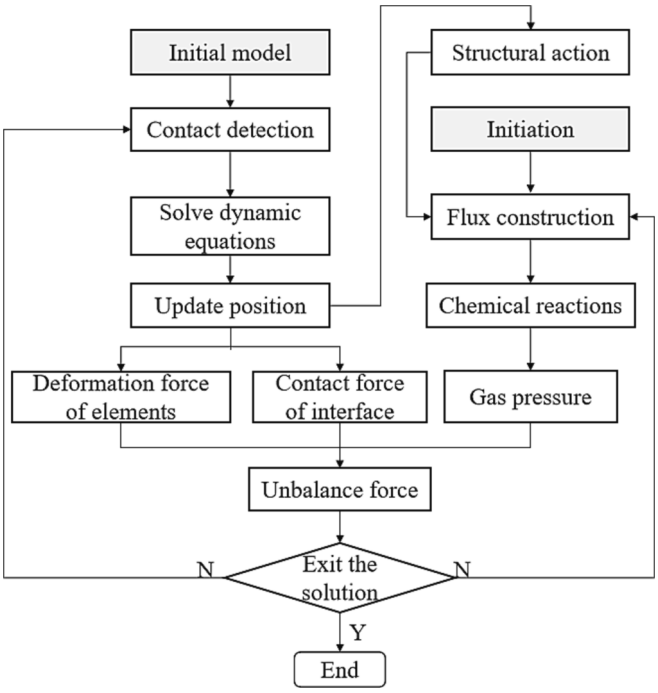

Fig. 11. The flowchart of the coupling algorithm of rock and blasting gas.

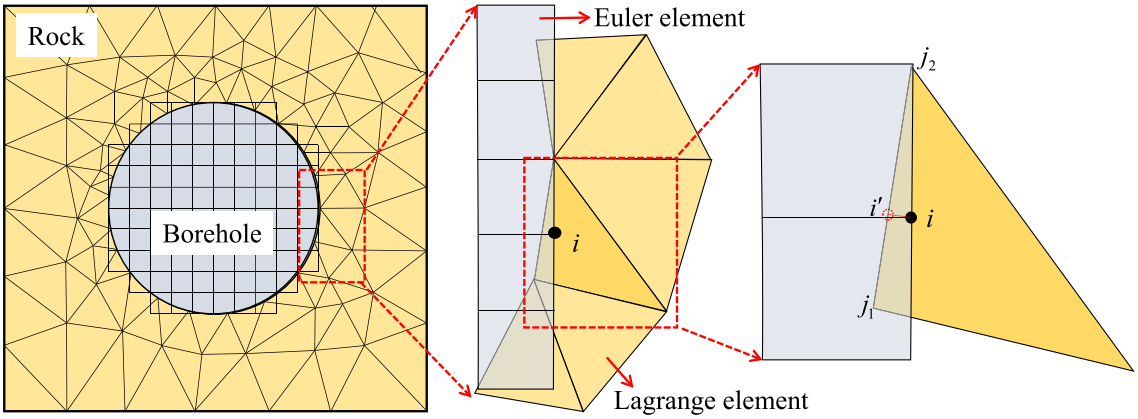

Fig. 10. The pressure interpolation calculation diagram at the fluid–structure interaction boundary.

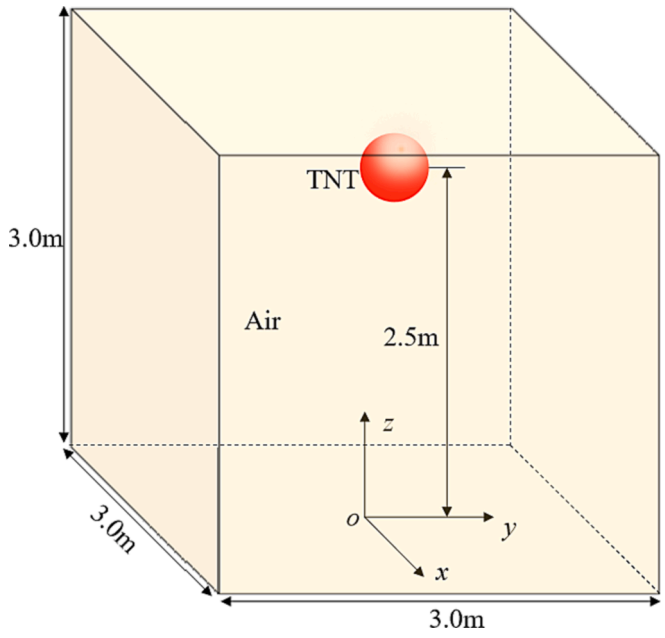

Fig. 12. Numerical model.

numerical method, the cube air domain is shown in Fig. 12, the cube size is 3.0 m × 3.0 m × 3.0 m, and the spherical TNT explosive which mass is 8 kg is set at 2.5 m above the air domain. The whole calculation domain is divided by regular hexahedral grid, with a grid number of 729000, where air pressure is 101 kPa, density is 1.02 kg/m^3, and TNT density is 1630 kg/m^3. All free surfaces are set as no reflective boundaries during calculation.

For the calculation of the peak pressure of the shock wave, some relevant empirical formulas were summarized previously. For example, Brode (1955) gave the peak empirical formula of near-earth blasting in air as follows:

$$\begin{aligned} P_{s0} &= 0.67Z^{-3} + 0.1, && (Z > 1) \\ P_{s0} &= 0.098Z^{-1} + 0.1455Z^{-2} + 0.585Z^{-3} - 0.0019, && (0.01 \leqslant Z \leqslant 1) \end{aligned} \tag{9}$$

Baker (1973) summarized the empirical formula for over-pressure peak value for spheroid TNT packs:

$$\begin{aligned} P_{s0} &= 20.04Z^{-1} + 1.94Z^{-2} - 0.04Z^{-3}, && (0.05 \leqslant Z \leqslant 0.5) \\ P_{s0} &= 0.67Z^{-1} + 3.01Z^{-2} + 4.31Z^{-3}, && (0.5 < Z < 70.9) \end{aligned} \tag{10}$$

Henrych (1979) based on the basis of comparing the research results of other scholars and combining with the TNT blasting experimental data, an empirical formula for describing the peak decay law of blasting wave in the self-use air domain:

$$\begin{aligned} P_{s0} &= 1.4072Z^{-1} + 0.544Z^{-2} - 0.0357Z^{-3} + 0.0000625Z^{-4}, && (0.1 \leqslant Z \leqslant 0.3) \\ P_{s0} &= 0.619Z^{-1} - 0.033Z^{-2} + 0.213Z^{-3}, && (0.3 < Z \leqslant 1) \\ P_{s0} &= 0.066Z^{-1} + 0.405Z^{-2} + 0.329Z^{-3}, && (1 < Z \leqslant 10) \end{aligned} \tag{11}$$

In the above equation, P_{s0} is the peak over-pressure (MPa) and Z is the proportional distance(m/kg$^{1/3}$).

The cloud map of shock wave pressure evolution obtained by the method proposed in this paper is shown in Fig. 13. The figure shows that the shock wave diffuses to the periphery in the form of a sphere, and the over-pressure peak gradually decreases with the increase of time. With the over-pressure belt as the boundary, the outer pressure of the over-pressure surface is the atmospheric pressure, and the negative pressure cavity appears inside the over-pressure surface. The peak pressure at different distances from the blasting center is extracted, and the comparison with the results obtained by the empirical formula is shown in Fig. 14, which shows that the results obtained in this paper are basically consistent with the solution of the empirical formula, so as to verify the validity of the calculation method in this paper.

5. Damage and stress evolution in the numerical simulation

5.1. Numerical model establishment

A numerical model of the rock specimen, identical in size to the one

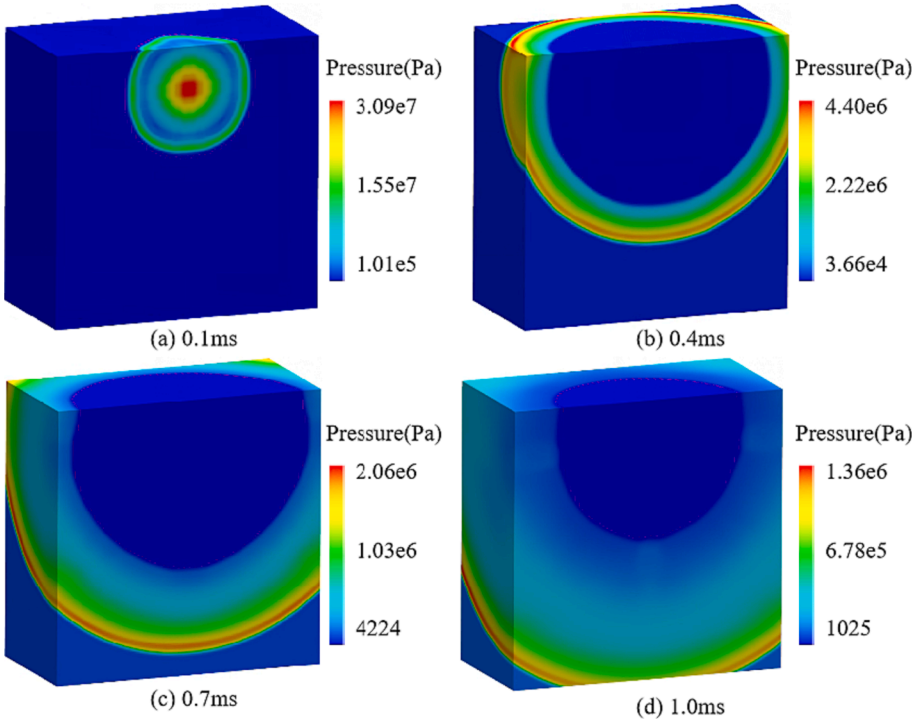

Fig. 13. Cloud map of shock wave pressure evolution.

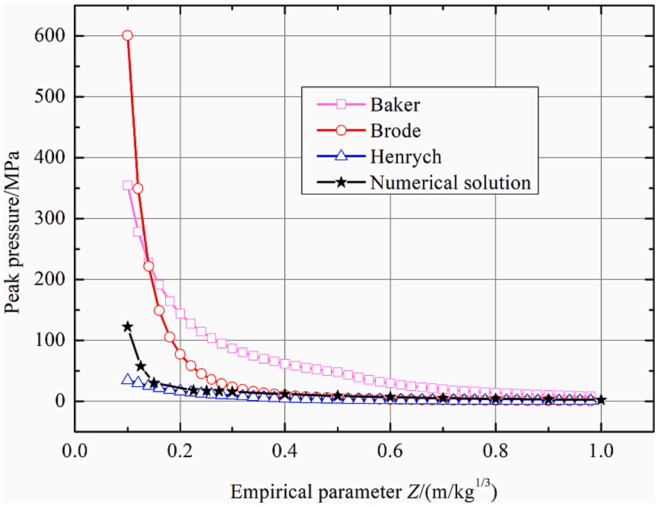

Fig. 14. Change of over-pressure peak with proportional distance.

used in the experimental model, is established as shown in Fig. 15. This model consists of 83,661 tetrahedral grids, with a minimum grid size of 0.3 mm. The air and explosives are represented by Euler orthogonal grids, with the explosive positioned as described in the three experimental groups mentioned earlier. Throughout the calculation process, the explosive density is set at 1000 kg/m^3, and the initial blasting pressure is 120 MPa. To simplify the calculation, Young's modulus is employed to describe both the rock specimen and the blasthole stemming, with their mechanical parameters provided in Table 4. The numerical simulation is also divided into three groups, corresponding to specimen A, specimen B, and specimen C, which align with the experimental model.

5.2. Propagation process of blasting gas and evolution of the rock mass damage

Dividing the numerical model along the central axis allows to obtain cloud maps of the evolution of blasting gas pressure and the distribution of specimen damage at different times, as depicted in Fig. 16. Since the air interval length is the same between specimen A and specimen C, it takes the same time (t = 54 μs) for the blasting gas in specimen A to reach the bottom of the blasthole as it takes for specimen C to reach the top of the blasthole. On the other hand, due to the smaller air-deck length on both sides of the explosive in specimen B, the blasting gas reaches the upper and lower ends of the blasthole at t = 30 μs. As the blasting gas propagates, local damage first appears in the radial direction of the charge segment. Subsequently, as the blasting gas reaches the end of the blasthole, damage starts to appear at the end position. The damage in the charge segment continues to expand, and then the blasting gas reflects and propagates back at t = 300 μs. At this point, the pressure attenuation of the blasting gas becomes severe enough to cause further damage to the rock specimen, resulting in maximum damage. The overall damage distribution characteristics of the numerical model can be summarized as follows: tensile failure is mainly observed in the near area of the blasthole, while shear failure is predominantly observed in the far area. Additionally, the damage range in the charge segment is greater than that in other areas.

In numerical calculations, the damage degree of the solid is defined as:

$$\overline{D}_b = \frac{V_b}{V_T} \tag{12}$$

where V_b represents the total volume of solid destroyed in the numerical model (m^3); V_T denotes the volume of all solids in the numerical model (m^3). When the cohesion and tensile strength of the solid both decrease to 0, it is considered that the solid has failed.

The damage degree curves of the three specimen groups over time are depicted in Fig. 16 (d). It can be observed from the figure that prior to t = 50 μs, the damage degree of all three specimen groups exhibits a

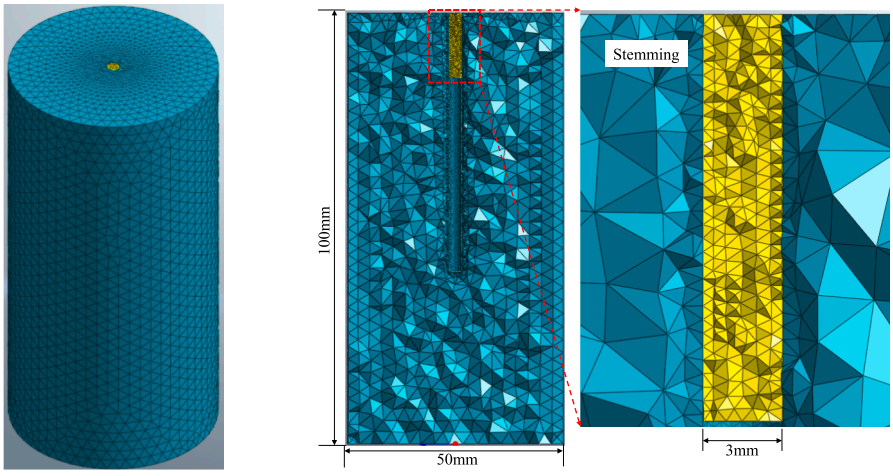

(a) numerical model grid (b) Profile along the blasthole axis

Fig. 15. Numerical model of the rock specimen.

Table 4
Mechanical parameters of the rock specimen and blasthole stemming.

Material	Density (kg/m^3)	Elastic modulus (GPa)	Poisson's ratio	Cohesive force (MPa)	Tensile strength (MPa)	Internal friction angle (°)
Rock specimen	2500	12	0.25	12	6	35
Blasthole stemming	2000	5	0.25	6	3	35

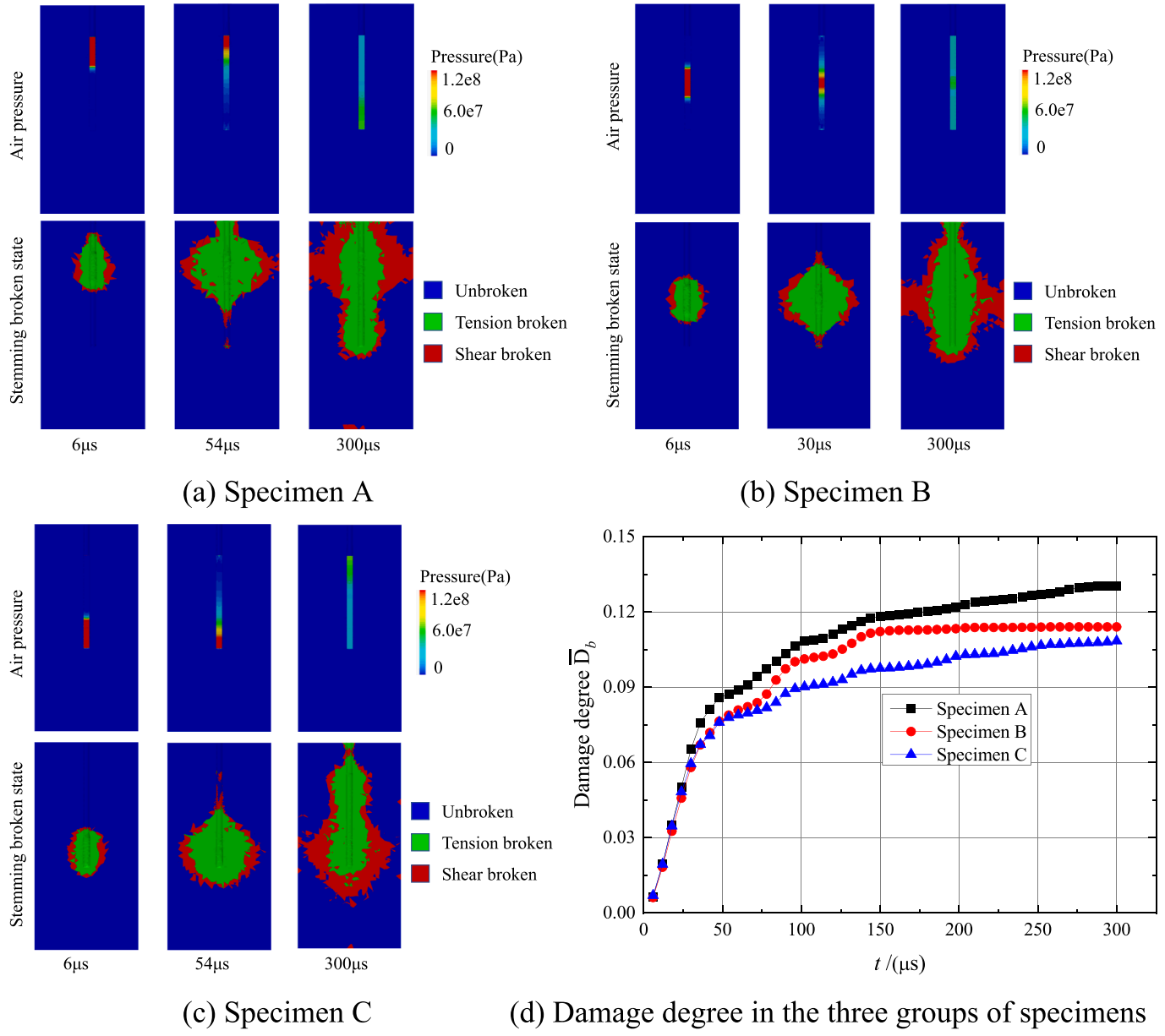

Fig. 16. Propagation of blasting gas and evolution of damage in specimens.

rapid increase, followed by a gradual slowdown and stabilization. Around $t = 50$ μs, the blasting gas reaches the end of the blasthole, and the initial interaction between the gas and rock becomes the primary factor influencing rock damage and failure. Subsequent reflection and transmission of the blasting gas have a relatively minor impact on rock damage and failure. Notably, there are differences in the final blasting damage effects between the numerical simulation results and the experimental results. Among the three specimen groups in the numerical simulation, specimen A exhibits the highest damage degree, while specimen C has the lowest damage degree. There are a couple of reasons for the differences between the numerical simulation and the model experiment. Firstly, in the model experiment, there is an actual dynamic expansion process of internal cracks within the specimen under the influence of the blasting load and the dissipation effect of the blasting gas. In contrast, the numerical model treats the rock as a continuum, where the damage of the element is equivalent to crack generation. This discrepancy accounts for the variation in the damage degrees observed. Secondly, in order to enhance computational efficiency, the numerical simulation assumes that the initial contact between the blasting gas and the rock is the primary factor leading to specimen failure. Consequently, in the Euler fluid calculations, the contact surface between the blasting gas (fluid) and the rock (solid) is treated as a rigid surface without considering the deformation of the solid portion. These factors collectively contribute to the disparities between the numerical simulation results and the model experimental results.

5.3. *Stress evolution characteristics of different segments*

The evolution of Mises stress in the three specimen groups is depicted in Fig. 17. Referring to the blasting gas pressure evolution cloud diagram in Fig. 16, it can be observed that the initial stress in the charge segment is the highest, followed by the propagation of stress waves towards the blasthole and its surrounding areas. At $t = 54$ μs, stress response begins to manifest at the blasthole ends of both specimen A and specimen C. However, for specimen B, the stress response occurs earlier at $t = 30$ μs, preceding that of specimen A and specimen C. The stress evolution process inside the blasthole for the three specimen groups aligns closely with the diffusion process of the blasting gas. Notably, due to the direct

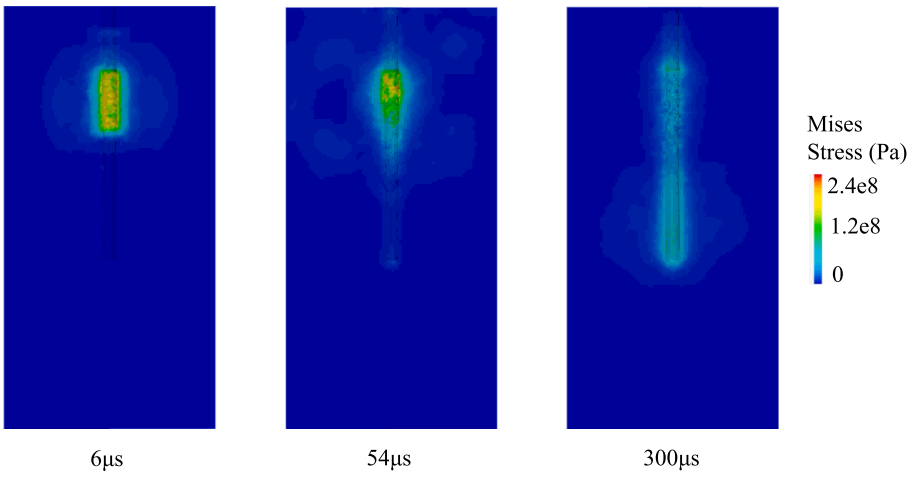

(a) Specimen A

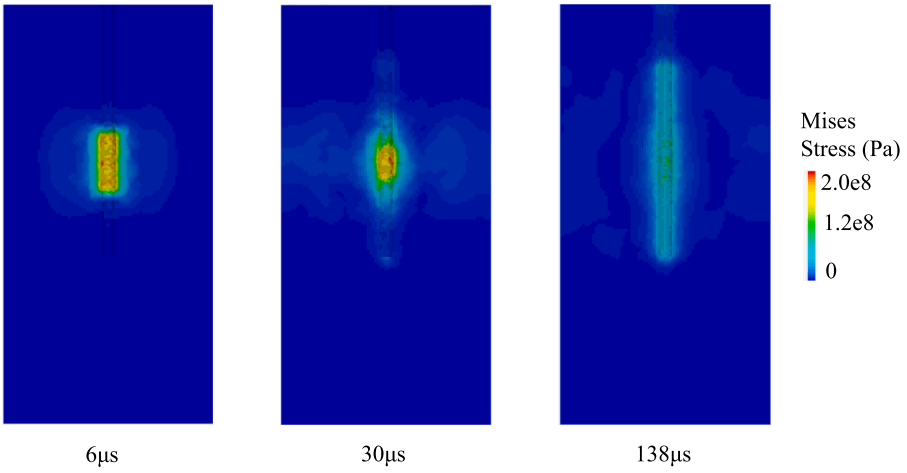

(b) Specimen B

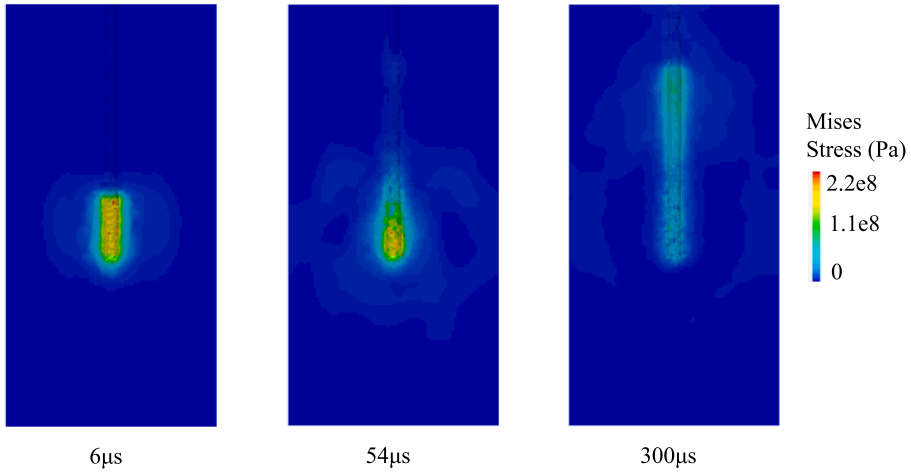

(c) Specimen C

Fig. 17. Mises stress evolution cloud map of the three specimen groups.

impact of the blasting gas on the blasthole wall, the Mises stress value in the blasthole wall is significantly higher compared to other positions within the specimen.

By calculating the average Mises stress values at the charge segment and the blasthole end for the three specimen groups, the time history curves are plotted as shown in Fig. 18. It should be noted that for specimen A and specimen B, the blasthole end refers to segment IV, while for specimen C, the blasthole end refers to segment II. Due to the symmetry of the charge segment positions in specimen A and specimen C, the time history curves of the Mises stress for the charge segment and the blasthole end in the two groups of specimens exhibit a high degree of consistency.

For the charge segment, the Mises stress of specimen A and specimen C exhibits an overall trend of rapid increase followed by a slow decrease. The rise section of Mises stress in specimen B is similar to that of specimen A and specimen C, but the decline section is significantly lower compared to the other two groups of specimens. The main reason for this difference is that the charge segment of specimen B is positioned in the middle of the blasthole, allowing the blasting gas to escape to both sides of the blasthole simultaneously. As a result, the expansion volume of the blasting gas in specimen B is larger than that in specimen A and specimen C at the same time, leading to a lower corresponding blasting gas pressure. At $t = 225$ μs, the Mises stress of specimen B transitions from decreasing to increasing. By $t = 300$ μs, its stress value slightly surpasses that of specimen A and specimen C. This change is primarily caused by the reflection and transmission of the blasting gas from the blasthole end of specimen B, where it converges and overlaps in the middle of the blasthole.

For the blasthole end, the Mises stress of specimen A and specimen C exhibits an overall increasing trend and gradually stabilizes after $t = 250$ μs. Specimen B, on the other hand, has a smaller air-deck length in the blasthole compared to specimen A and specimen C. Consequently, once the blasting gas reaches the blasthole end, the blasting gas pressure in specimen B is higher than that in specimen A and specimen C. As a result, the Mises stress value of specimen B is correspondingly higher than that of the other two groups. After $t = 138$ μs, the stress value of specimen B starts to decrease, primarily due to the reflection, transmission, and dissipation of the blasting gas from the blasthole end.

6. Conclusions

In this paper, indoor model experiments and numerical simulation methods are employed to analyze the evolution of blasting stress, damage distribution, and blasting fracture characteristics in rock specimens. The research focuses on the air-deck charge blasting technology, with particular emphasis on the effect of blasting gas. The main findings are summarized as follows:

(1) Model experiment: Three groups of air-deck charge blasting model experiments were conducted. During the blasting process, a group of divergent radial cracks originated at the center of the blasthole, resulting in the separation and fragmentation of the rock mass. Among them, specimen C exhibited the highest damage degree in the charge segment (segment IV), reaching 0.815. On the other hand, the stemming segment (segment I) of specimen C showed the smallest damage degree, measuring only 0.672. Furthermore, in specimen B, the blasting gas generated by the detonation of explosives acted on the bottom segment after being buffered by the air-deck. This reduced the impact strength while prolonging the action time, thereby facilitating crack initiation and continuous propagation. As a result, the damage degree in the bottom segment of specimen C was lower compared to specimen B. The comparison between specimen A and specimen B also indicates that there exists an optimal range for the air-deck length, which should be determined based on engineering requirements. In summary, the comparative analysis of the damage characteristics in the charge segment, stemming segment, and bottom segment of the three groups of specimens reveals that the primary factors determining the distribution characteristics of damage are the position of the charge segment, and the length and position of the air-deck.

(2) Numerical simulation: The Lagrangian finite element method is employed to describe the dynamic changes in the stress field within a solid medium, while the Euler finite volume method is used to simulate the evolution and diffusion process of the pressure field generated by blasting gas. The coupling of these two methods enables the numerical simulation of air-deck charge blasting, considering the physical process of gas diffusion. The analysis reveals that the failure near the blasthole, under the influence of the blasting gas, is primarily characterized by tensile failure, whereas shear failure predominates in the distant regions. During the rock fragmentation process caused by the blasting gas, the initial interaction between the blasting gas and the rock is the main factor influencing rock damage and failure, while subsequent gas reflection and transmission have a relatively minor impact. The evolution of Mises stress exhibits variations between the charge segment and the blasthole end in the three specimen groups. The Mises stress in the charge segment of all three groups shows an overall pattern of rapid increase followed by a slower decrease, with specimen B displaying a more rapid decay in Mises stress. Additionally, compared to specimen A and specimen C, the Mises stress at the blasthole end in specimen B decays earlier, primarily due to the reflection, transmission, and dissipation of the blasting gas from the blasthole end.

7. Discussions

The fracturing of rocks during blasting is attributed to the combined effects of blasting stress wave and blasting gas, which is a widely accepted conclusion in the current foundational theory of rock blasting. With advancements in experimental techniques and the enhancement of

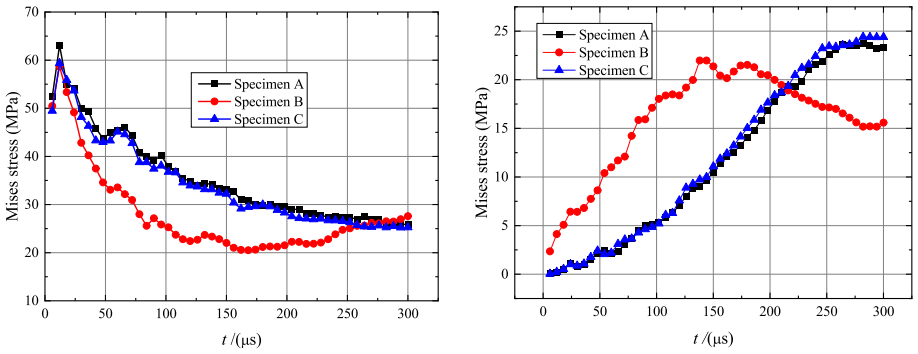

(a) Chage segment (b) Blasthole end

Fig. 18. Time history curve of Mises stress evolution.

software/hardware capabilities, both experimental and numerical simulation research on rock blasting have entered a phase of significant development. The investigation of the impact of blasting stress waves on rock fragmentation has emerged as a prominent topic in recent years, while the role of blasting gas, which serves as the primary energy source for rock fracture, has received relatively less attention.

In terms of experimental research, whether it involves two-dimensional or three-dimensional model experiments, the propagation and attenuation behavior of blasting stress wave can be studied phenomenologically and quantitatively using techniques such as high-speed photography technology, ultra dynamic strain testing, and digital image correlation. These experimental methods are typically considered as "far field" testing approaches. However, the expansion and dissipation process of blasting gas within the blasthole, as well as its gas wedge effect on cracks, remain "invisible and untouchable". These aspects require experimental testing techniques that can adapt to the high temperature and high-pressure environment near the blasthole during the blasting process and achieve "near field" testing. Undoubtedly, this poses significant challenges. The analysis of the effects of blasting gas presented in this paper, which utilizes CT scanning and 3D reconstruction technology, constitutes a post-blasting effect analysis. It is a deductive analysis that still necessitates verification and support from "near field" test data. Quantitatively analyzing the action of blasting gas at the experimental level still has a long way to go.

In terms of numerical simulation, the current main methods are the finite element method and finite difference method based on continuum mechanics. These methods are suitable for solving and analyzing continuous processes, such as the propagation and attenuation of blasting stress waves, thereby providing methodological support for studying the effects of blasting stress waves. However, due to the complexity of physical processes such as the expansion and dissipation of blasting gas, accurately depicting the process of rock fragmentation induced by blasting gas remains challenging for these numerical simulation methods. The current commercial software such as LS-DYNA, AUTODYN etc. can complete the numerical simulation of rock fracture under the coupling action of stress wave and explosive gas to some extent. A novel numerical simulation method that couples the Lagrangian finite element and the Euler finite volume is proposed in the framework of CDEM to complete the rock blasting simulation in this paper. Specifically, the Lagrangian finite element method is employed to describe the dynamic changes in the stress field of the rock medium, while the Euler finite volume method is used to simulate the evolution and diffusion process of the pressure field of the blasting gas. This approach allows for preliminary numerical simulation research on blasting-induced fracture, considering the effects of blasting gas. It should be noted that the focus of the numerical simulation in this paper is to highlight the rock fragmentation effects of blasting gas, providing valuable insights for understanding the mechanisms of rock breaking by blasting gas. Consequently, the simulation does not incorporate the effects of blasting stress waves. The primary aim of the numerical simulation in this study is to explore research methods rather than to directly validate the model experimental results.

Funding information

This research was supported by: (1) National Natural Science Foundation of China (52204085); (2) Interdisciplinary Research Project for Young Teachers of USTB (Fundamental Research Funds for the Central Universities) (FRF-IDRY-21–006); (3) Foundation of Hubei Key Laboratory of Blasting Engineering (BL2021-05).

CRediT authorship contribution statement

Chenxi Ding: Writing – original draft, Methodology, Software. **Renshu Yang:** Conceptualization, Supervision. **Xinguang Zhu:** Writing – original draft, Validation. **Chun Feng:** Visualization, Software. **Jun Zhou:** Writing – review & editing.

Declaration of Competing Interest

The authors declare that they have no known competing financial interests or personal relationships that could have appeared to influence the work reported in this paper.

Data availability

No data was used for the research described in the article.

References

Baker, W.E., 1973. Explosions in Air. University of Texas Press, Austin, USA.
Brode, H.L., 1955. Numerical solution of spherical blast waves. J. Appl. Phys. 26 (6), 766–775.
Cheng, R.S., Zhou, Z.L., Chen, W.S., Hao, H., 2022. Effects of axial air deck on blast-induced ground vibration. Rock Mech. Rock Eng. 55 (2), 1037–1053.
Costamagna, E., Oggeri, C., Segarra, P., Castedo, R., Navarro, J., 2018. Assessment of contour profile quality in D&B tunnelling. Tunn. Undergr. Space Technol. 75, 67–80.
Ding, C.X., Yang, R.S., Lei, Z., Wang, M., Zhao, Y., Lin, H., 2021. Fractal damage and crack propagation in decoupled charge blasting. Soil Dyn. Earthq. Eng. 141, 106503.
Ding, C.X., Yang, R.S., Chen, C., Zhu, X.G., Feng, C., Xie, Q.M., 2022. Space-time effect of blasting stress wave and blasting gas on rock fracture based on a cavity charge structure. Int. J. Rock Mech. Min. Sci. 160, 105238.
Fang, S.Z., Li, W.Y., Yang, Y., Chen, C., Xu, P., 2023. Experimental study on the dynamic mechanical behavior and energy dissipation characteristics of deep rock under coupled impact loading and hydrostatic pre-stress. J. Vib. Shock 42 (6), 280–288.
Gao, F., Tang, L.H., Yang, C., Yang, P.L., Xiong, X., Wang, W.F., 2023. Blasting-induced rock damage control in a soft broken roadway excavation using an air deck at the blasthole bottom. B. Eng. Geol. Environ. 82 (3), 97.
Gu, W.B., Wang, Z.X., Chen, J.H., Liu, J.Q., Lu, M., 2015. Experimental and theoretical study on influence of different charging structures on blasting vibration energy. Shock Vib. 248739.
Han, H., Fukuda, D., Liu, H., Salmi, E.F., Sellers, E., Liu, T., Chan, A., 2020. Combined finite-discrete element modelling of rock fracture and fragmentation induced by contour blasting during tunnelling with high horizontal in-situ stress. Int. J. Rock Mech. Min. Sci. 127, 104214.
Hayat, M.B., Alagha, L., Ali, D., 2019. Air decks in surface blasting operations. J. Min. Sci. 55 (6), 922–929.
Henrych, J., 1979. The dynamics of explosion and its use. Elsevier Scientific Publishing Company, Amsterdam, Netherlands.
Huo, X.F., Qiu, X.Y., Shi, X.Z., Chen, H., Zong, C.X., Xie, C., 2023. Attenuation characteristics of blasting stress under decoupled cylindrical charge. Rock Mech. Rock Eng. 56, 4185–4209.
Ju, Y., Xi, C.D., Wang, S.J., Mao, L.T., Wang, K., Zhou, H.W., 2021. 3-D fracture evolution and water migration in fractured coal under variable stresses induced by fluidized mining: In situ triaxial loading and CT imaging analysis. Energy Rep. 7, 3060–3073.
Li, N., Chen, L.J., Zhang, P., 2006. Dynamic analysis for fracturing progress by detonation gas. Chin. J. Rock Mech. Eng. 28 (4), 460–463.
Li, X.D., Liu, K.W., Sha, Y.Y., Yang, J.C., Song, R.T., 2023. Numerical investigation on rock fragmentation under decoupled charge blasting. Comput. Geotech. 157, 105312.
Li, S.H., Zhao, M.H., Wang, Y.N., Rao, Y., 2004. A new numerical method for DEM-block and particle model. Int. J. Rock Mech. Min. Sci. 41 (3), 436.
Lin, F., Liu, R., Zhang, Z.G., Jiang, D.Y., Chen, J.H., Li, Y., 2021. Reduction of blasting induced ground vibrations using high-precision digital electronic detonators. Front. Earth Sci. 804504.
Liu, L., Katsabanis, P.D., 2020. Rock Fragmentation by Blasting. Taylor & Francis Group, London, UK.
Lou, X.M., Wang, Z.C., Chen, B.G., Yu, J., 2018. Theoretical calculation and experimental analysis on initial shock pressure of borehole wall under axial decoupled charge. Shock Vib. 7036726.
Lou, X.M., Zhou, P., Yu, J., Sun, M.W., 2020. Analysis on the impact pressure on blast hole wall with radial air-decked charge based on shock tube theory. Soil Dyn. Earthq. Eng. 128, 105905.
Lu, W., Hustrulid, W., 2003. A further study on the mechanism of airdecking. Fragblast 7 (4), 231–255.
Wang, Y.B., Wen, Z.J., Liu, G.Q., Wang, J.G., Bao, Z.Q., Lu, K.Q., Wang, D.C., Wang, B.Z., 2020. Explosion propagation and characteristics of rock damage in decoupled charge blasting based on computed tomography scanning. Int. J. Rock Mech. Min. Sci. 136, 104540.
Wu, L., Lu, W.B., Zhong, D.W., Zhu, H.B., 2010. Blasting mechanism of air-decked charge in concrete medium. Explo. Shock Wave. 30 (1), 58–64.
Xie, H.P., 1997. Mathematical foundation and method in fractal application. Science Press, Beijing, China.
Yang, R.S., Ding, C.X., Yang, L.Y., Lei, Z., Zhang, Z.R., Wang, Y.B., 2018. Visualizing the blast-induced stress wave and blasting gas action effects using digital image correlation. Int. J. Rock Mech. Min. Sci. 112, 47–54.
Yang, R.S., Ding, C.X., Yang, L.Y., Lei, Z., Zheng, C.D., 2019. Study of decoupled charge blasting based on high-speed digital image correlation method. Tunn. Undergr. Space Technol. 83, 51–59.

Yang, G.L., Yang, R.S., Jiang, L.L., 2012. Pressure distribution along borehole with axial air-deck charge blasting. Explo. Shock Wave. 32 (6), 653–657.
Yang, R.S., Zhao, Y., Fang, S.Z., Zhao, J., Wang, Y., Liu, Z., 2023. Effect of the detonation method on the stress field distribution and crack propagation of spacer charge blasting. Chin. J Eng. 45 (5), 714–727.
Yin, Z.M., Wang, X.G., Wang, D.S., Dang, Z.H., Bi, J.H., 2021. Analysis and application of stress distribution in 24-m high bench loosening blasting with axially uncoupled charge structure in Barun Open-pit Mine. Earth Env. Sci. 804, 022059.
Zhu, X.G., Feng, C., Cheng, P.D., Wang, X.Q., Li, S.H., 2021. A novel three-dimensional hydraulic fracturing model based on continuum-discontinuum element method. Comput. Method. Appl. Mech. Eng. 383, 113887.
Zhu, Z.M., Xie, H.P., Mohanty, B., 2008. Numerical investigation of blasting-induced damage in cylindrical rocks. Int. J. Rock Mech. Min. Sci. 45 (2), 111–121.